3D in-situ characterization reveals the instability-induced auxetic behavior of collagen scaffolds for tissue engineering

Enze Chen[1†], Byumsu Kim[2†], Nikolaos Bouklas[2✉], Lawrence J. Bonassar[2,3✉], and Stavros Gaitanaros[1✉]

[1]Department of Civil and Systems Engineering, Johns Hopkins University, Baltimore, MD 21218, USA
[2]Sibley School of Mechanical and Aerospace Engineering, Cornell University, Ithaca, NY 14850, USA
[3]Meinig School of Biomedical Engineering, Cornell University, Ithaca, NY 14850, USA,
†These authors contributed equally to this work

Collagen scaffolds seeded with human chondrocytes have tissue-engineering great potential for cartilage repair and regeneration. However, these porous scaffolds buckle under low compressive forces, generating regions of highly localized deformations that can cause cell death and deteriorate the integrity of the engineered tissue. We perform three-dimensional (3D) tomography-based characterization to track the evolution of collagen scaffolds' microstructure under large deformation. The results illustrate how instabilities produce a spatially varying compaction across the specimens, with more pronounced collapse near the free boundaries. We discover that, independent of differences in pore-size distributions, all collagen scaffolds examined displayed strong auxetic behavior i.e. their transverse area contracts under compression, as a result of the instability cascade. This feature, typically characteristic of engineered metamaterials, is of critical importance for the performance of collagen scaffolds in tissue engineering, especially regarding the persistent challenge of lateral integration in cartilage constructs.

Tissue Engineering | Collagen Scaffolds | 3D Characterization | Buckling

Correspondence:
Prof.Nikolaos Bouklas. Email: nb589@cornell.edu
Prof.Lawrence J. Bonassar. Email: lb244@cornell.edu
Prof.Stavros Gaitanaros. Email: stavrosg@jhu.edu

Introduction

Over the past three decades, tissue-engineered cartilage constructs have exhibited promising potential in restoring native tissue functionality (1). Currently available, or at a late stage of clinical trial, cartilage products (such as MACI®, Carticel®, and CMI) employ soft porous materials, such as collagen foams, to serve as scaffolding microstructures that provide initial attachment sites and mechanical support for chondrocytes (2–4). These scaffolds are designed to contain vertical pores to promote the generation of a matrix that mimics the oriented microstructure of native cartilage. The resulting mechanical properties of these collagen scaffolds are of significant importance in these biofabrication approaches, given that the tissue-engineered products undergo in vivo compression following implantation. Additionally, the Food and Drug Administration (FDA) guidance suggests that the mechanical characterization of engineered cartilage products is important in understanding implant performance (5). Despite the known importance of the underlying mechanics, no tissue-engineered cartilage products to this date have been able to recapitulate all mechanical properties of native tissue (6). Previous studies have highlighted the significant impact of morphological features of tissue-engineered cartilage on its micromechanical behavior and failure modes in the form of local strain concentrations (7). The latter have been shown to affect the viability of the cells seeded in the construct (9, 10). Collectively, these results indicate the need to quantify the effect of key microstructural features of collagen scaffolds on the resulting mechanical behavior of tissue-engineered cartilage constructs.

While previous findings have shed light on the correlation between the micromechanical environment and cell health, they primarily explored this behavior via two-dimensional (2D) analysis where 2D imaging and sample preparation impart artifacts on material behavior (7, 8). For example, buckling that occurs out of plane with respect to the field of view cannot be captured by the experimental 2D imaging technique. Further, to enable 2D imaging, samples must be sectioned, which changes the boundary conditions compared to the intact specimen. To overcome these challenges, non-destructive 3D imaging techniques utilizing micro-computed tomography (μCT) have been used to measure 3D deformation fields of porous material in situ (11, 12). However, these techniques have not been extensively applied to understand the mechanics of soft collagen foams.

The objective of this study is to investigate the interplay between the 3D porous microstructure and the corresponding nonlinear mechanics of collagen scaffolds through μCT imaging. We focus on commercially available porous collagen scaffolds made from bovine dermal type I collagen with honeycomb and sponge architectures (13, 14) manufactured from a freeze-drying process and examine their compressive behavior. In particular, we first perform microstructure characterization and use image analysis to extract key morphological features for both honeycomb and sponge scaffolds. In situ compressive experiments with sequential μCT scans are used to highlight deformation patterns, identify the corresponding critical buckling modes, and quantify the evolution of key microstructural features at different levels of macroscopic strain. Further, the μCT technique enables us to identify the microscopic mechanisms through which an emerg-

ing macroscopic auxetic response manifests. Establishing this auxetic response enables the identification of novel biomechanical mechanisms for implant failure. The in vivo reported data are vital for inverse-engineering cartilage constructs with tailored behavior at the post-buckling regime for optimal tissue regeneration.

Results

Microstructure characterization of collagen scaffolds. We first focus on quantifying key morphological features of collagen constructs with honeycomb and sponge microstructures. Figure 1(a) and Figure 1(b) show the reconstructed solid models extracted from the µCT stacks. Although both scaffolds share a similar quasi-2D tubular microstructure, the associated pores have distinct characteristics. Using 2D section images from approximately the mid-height of each specimen, we extract the distributions of four structural descriptors that have been shown (15–17) to greatly influence the resulting mechanical properties of porous materials: (i) wall thickness, (ii) pore area, (iii) pore compactness, and (iv) neighbor distance. Figure 1(c) illustrates the mean wall thickness for each scaffold across the specimen height. The results reveal that there are no significant density gradients across each specimen, with the wall thickness for both scaffolds being nearly constant throughout their thickness. The honeycomb construct is shown to have a slightly higher average wall thickness (6.42µm) than the sponge scaffold (6.34µm). Dividing the height of each specimen (~1.2mm) with the corresponding mean wall thickness gives a slenderness ratio of 175 and 189 for the honeycomb and the sponge respectively. These values confirm that under compression, buckling will be the governing deformation mechanism. The distribution of pore areas for the two collagen constructs is displayed in Figure 1(d). The honeycomb scaffold exhibits two notable peaks at approximately 39520 μm^2 and 16750 μm^2. On the contrary, there is a significantly larger number of smaller pores within the sponge scaffolds, resulting in a single peak of the distribution at 5025 μm^2 area. Despite the differences in pore-size distributions, the shape of the pores in both structures is similar, as indicated by the compactness metric distribution shown in Figure 1(e). The honeycomb demonstrates an average compactness of 0.68±0.16, slightly higher than the corresponding values for the sponge (0.66±0.14). These values indicate that most of the pores in the collagen scaffolds are not quite circular, since their compactness is closer to the one of a square, $\pi/4$. Finally, in Figure 1(f) we report the pore neighbor distance distribution for both types of scaffolds. The honeycomb displays a smoother distribution than the sponge scaffold due to the larger and more uniform size of its pores. Furthermore, in both honeycomb and sponge scaffolds the neighbor distance seems to be independent of location within the sectional area, indicating homogeneous pore distributions within the structures.

In-situ Testing and Deformation. Figure 2(a) illustrates the evolution of collapse for a collagen scaffold with honeycomb structure at six levels of applied macroscopic strain. To capture the complex and multi-scale nature of the involved deformations, we extract images of the 3D reconstructed specimens (top) as well as 2D sections across all three directions (bottom) for all increments of the compressive loads. Initially, the walls of the undeformed scaffold remain nearly straight through at an inclined angle with respect to the compressive direction. In step 2, with an applied strain close to 8.5%, the walls of certain cells near the boundary start buckling into the scaffold, as observed from the 1-1 and 2-2 sections (see circled regions). Contrary, most cell walls within the structure retain their initial orientation. With increasing compression (22.5%), collapse of pores propagates towards the interior of the cellular microstructure. These deformations at the cell level cause a notable reduction in the cross-sectional area of the whole specimen, as clearly evident from the corresponding top view. As the compaction of pores grows significantly (>30%), contact between neighboring walls provides additional support and prevents the further propagation of collapse near the center of the scaffold.

To examine the local deformation of scaffold walls and their spatial dependence, we extract two clusters of cells, one near the center (marked with red) and one close to the boundary (marked with yellow) and monitor their individual structural evolution during compression (Figure 2(b)). It is seen that the central pores mainly maintain their overall shape, even for large macroscopic strains, depicting a uniform manner of collapse through the wrinkling of the scaffold walls. In contrast, the boundary cells show significant local and global deformations at similar levels of compression, which in turn result in increased pore compaction.

We subsequently repeat the in-situ testing and monitoring process for scaffolds with a sponge microstructure (Figure 3). It is again observed that the thin walls of the scaffold are initially straight, however in this case they also appear to be nearly vertical i.e. displaying a less pronounced inclination with respect to the loading axis than the walls of the honeycomb scaffold. At imaging level 3, corresponding to a macroscopic strain of approximately 30%, we clearly observe the buckling of boundary cells in the 1-1 and 2-2 sections. Interestingly, the deformation of the cell walls varies in the vertical direction too, with the appearance of walls that have localized near the bottom as well as ones that collapsed at mid-height. As compression progresses, the bottom region continues to collapse due to buckling causing a shift of the scaffold as evidenced in the 1-1 section. Imaging in the 2-2 sections reveals an inward-type of folding mechanism that results in an overall decrease of the specimen cross-sectional area. Figure 3(b) illustrates the corresponding evolution of pore morphology for clusters close to the center (red) (top) and boundary (bottom) (yellow). In a similar manner to the honeycomb construct, the pores located closer to the center maintain their shape to a greater extent than those near the boundary that experience significant compaction and appear nearly densified at 47% strain.

We further exploit the tomography imaging from the in-situ tests to extract the evolution of structure characteristics at

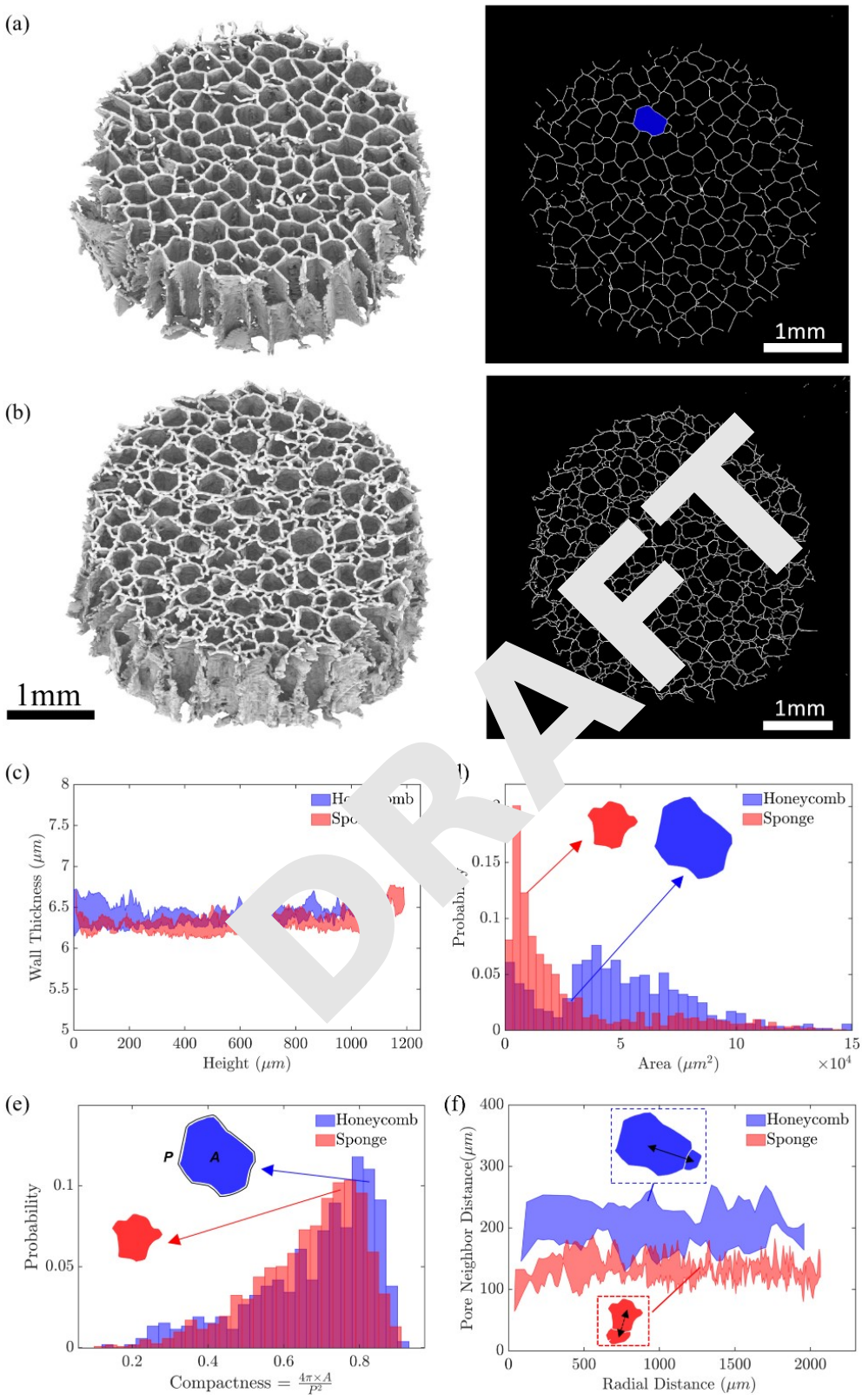

Fig. 1. Tomography-based structure characterization of collagen constructs. (a) Reconstructed 3D solid model (left) and cross-sectional slice at mid-height (right) for a scaffold with honeycomb structure. (b) Reconstructed 3D solid model (left) and cross-sectional slice at mid-height (right) for a collagen scaffold with sponge structure. (c) Mean wall thickness across the specimens' heights. (d) Pore area distributions. (e) Pore compactness distributions. (f) Neighbor distance as a function of radial distance.

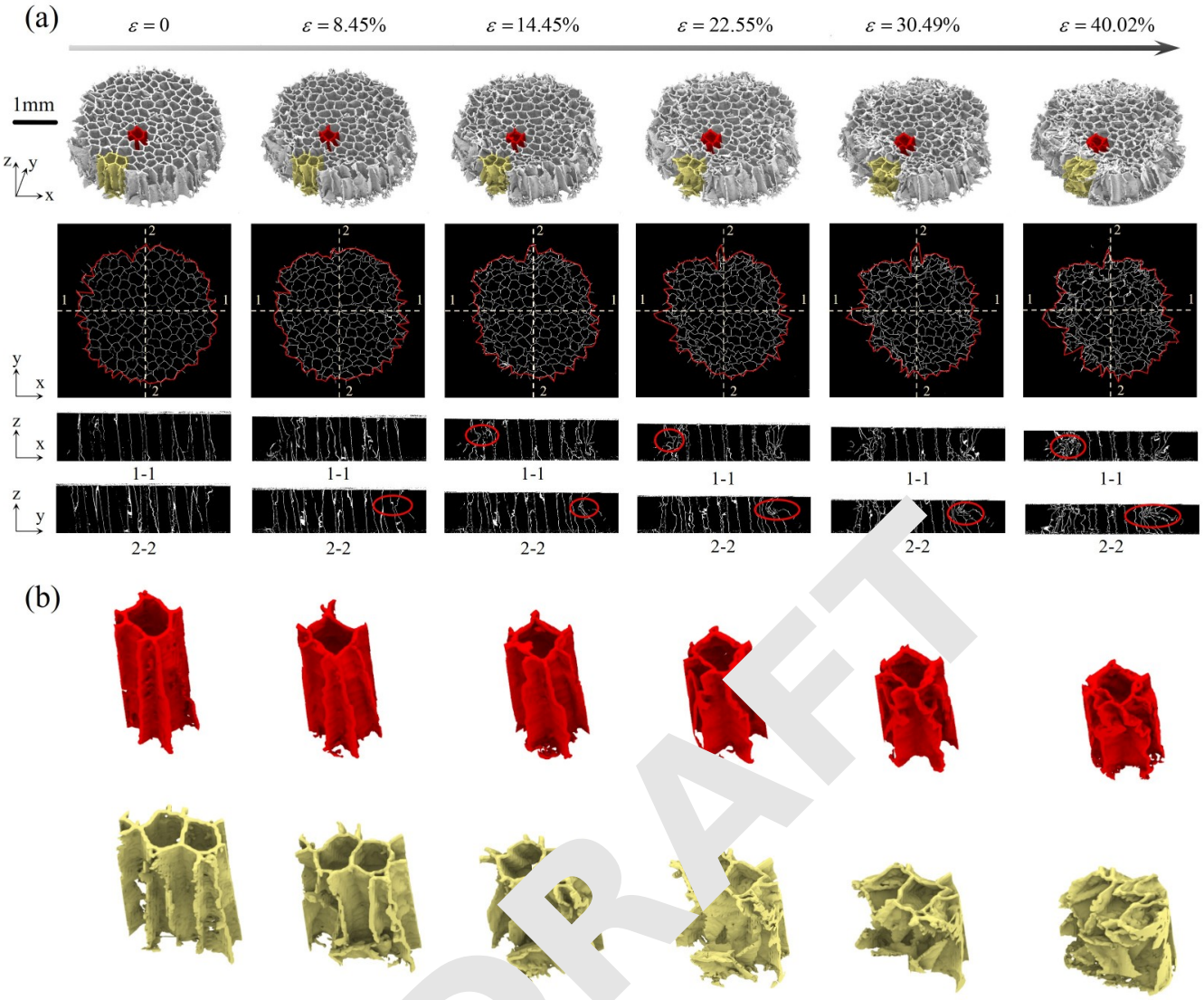

Fig. 2. In-situ buckling and localization in honeycomb construct. (a) Imaging of large deformation evolution through (top to bottom) reconstructed 3D solid models, cross-sectional slices at mid-height, and transverse slices at six levels of applied macroscopic strain. (b) Buckling of cell walls and deformation of pores near the center (red) and the boundary (yellow).

different levels of deformation for both the honeycomb (Figure 4(a-d)) and sponge (Figure 4(e-h)) scaffolds. To examine the spatially varying collapse of pores, we measure the pore area (Figure 4(a/e)) and pore neighbor distance (Figure 4(b/f)) as a function of radial distance from the center. In both cases, the corresponding distributions for the undeformed and highly deformed scaffold are compared. It is evident that the collapse of pores results in a significant reduction in both morphological descriptors, regardless of the particular scaffold morphology. Furthermore, this decrease is more pronounced at distances larger than 1mm from the center of the specimen. These findings provide quantitative evidence of the observations made based on the 3D reconstructed images shown in Figure 2(a) and Figure 3(a). Figure 4(c) and Figure 4(c) depict the specimens' cross-sectional areas, corresponding to the domain enclosed by the red curve in Figure 2(a)-Figure 3(a), as a function of height, for six increments of the applied strain. A key observation that is common for both microstructures involve the decrease of macroscopic area with increasing deformation. However, there is a notable difference between them. The honeycomb structure displays a non-uniform cross-sectional area across its height, characterized by a clear dip in the middle. This variation arises from buckling occurring at the structure's mid-height, leading to a significant area reduction in these regions. Conversely, the sponge structure maintains a more consistent cross-sectional area distribution throughout its height but has the lowest area near the bottom boundary. The sponge's area distribution is attributed to its buckling location near the base and slanted shape in post-buckling, which concentrates the buckling at its lower boundary. This results in a uniform area reduction in the other regions. As a result, the distribution

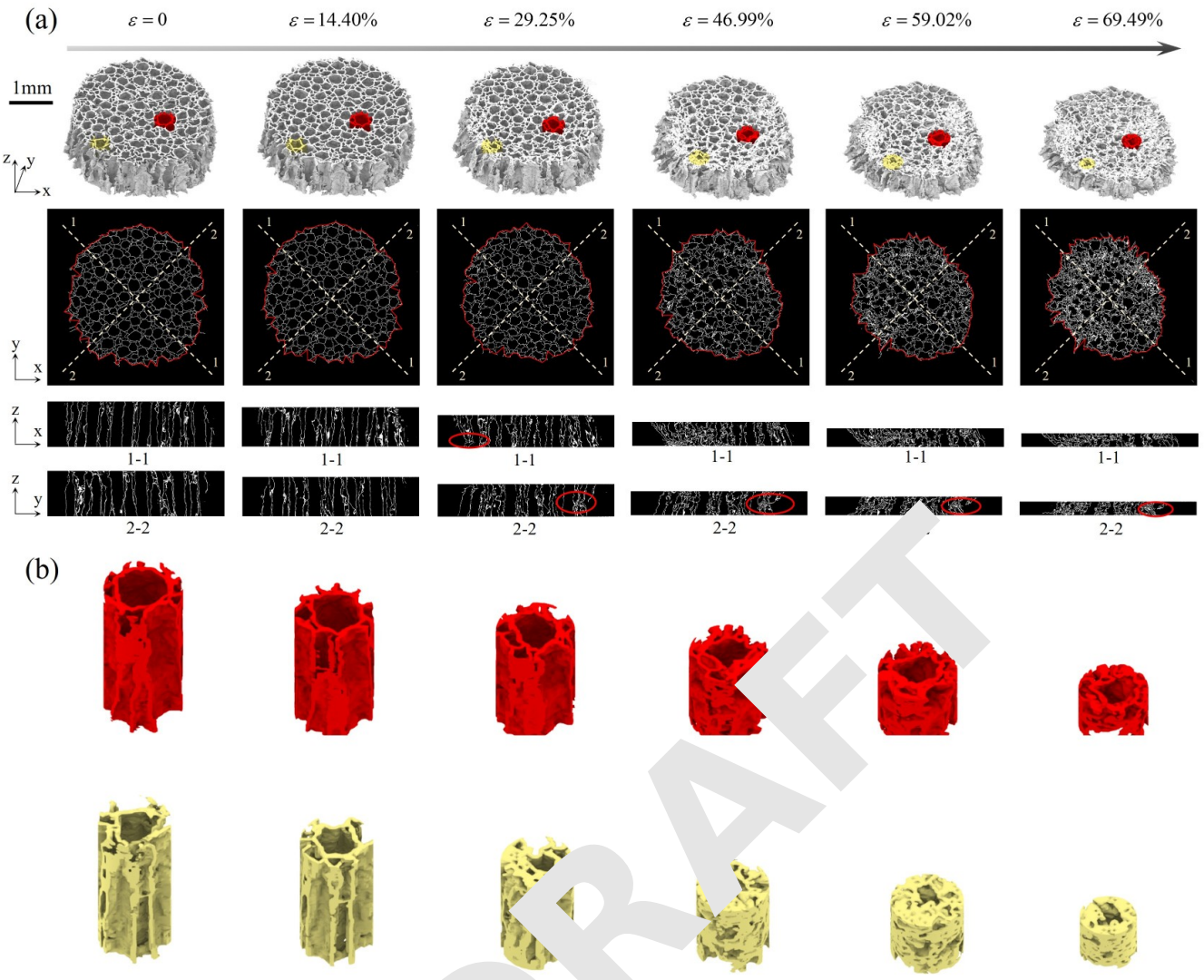

Fig. 3. In-situ buckling and localization in sponge construct. (a) Imaging of large deformation evolution through (top to bottom): reconstructed 3D solid models, cross-se slices at mid-height, and transverse slices at six levels of applied macroscopic strain. (b) Buckling of cell walls and deformation of pores near the center (red) and the bo (yellow).

the cross-sectional area highly correlates with the buckling location and post-buckling behavior and can be used to probe the deformation of the scaffold.

To further examine the compaction of the scaffold under compression, we analyzed the volume fraction in various regions based on the radial distance for both honeycomb and sponge, as shown in Figure 4(d) and Figure 4(h). Both structures share one key observation of heterogeneous volume compaction in the radial direction. Initially, both structures exhibit nearly uniform volume fractions radially. However, as compression continues, volume fraction increases more significantly farther from the center. Specifically, regions beyond a radial distance of 700µm display a pronounced jump in volume fractions when highly compressed. In honeycomb structures, regions up to 700µm from the center see an average volume fraction increase of 74% from its original state to a 40% compressed state. In contrast, areas beyond 700µm experience a much higher volume fraction increase of 122%. For sponges, the central regions only exhibit an average 91% growth in volume fraction, while the volume fraction shows a 133% increase in the outer regions. This finding quantitatively confirms the scaffold's non-uniform compaction and concentrated deformation caused by the instability at the boundary and the post-buckling behavior observed in Figure 2 and Figure 3.

Nonetheless, the significant reduction of specimen area with increasing compaction seems to be a feature that is independent of the specific scaffold morphology. To highlight this feature, we plot for all collagen scaffolds tested, their cross-sectional area at mid-height A, normalized by its undeformed value A_0, as a function of the applied strain (see Figure 5(a)). It is obvious that all specimens see a decrease that for a 40% strain varies between 5-25%, result indicates a strong auxetic behavior of collagen constructs, that is very different than typical monolithic solids that expand in the direction of the compressive loads. To illustrate the striking

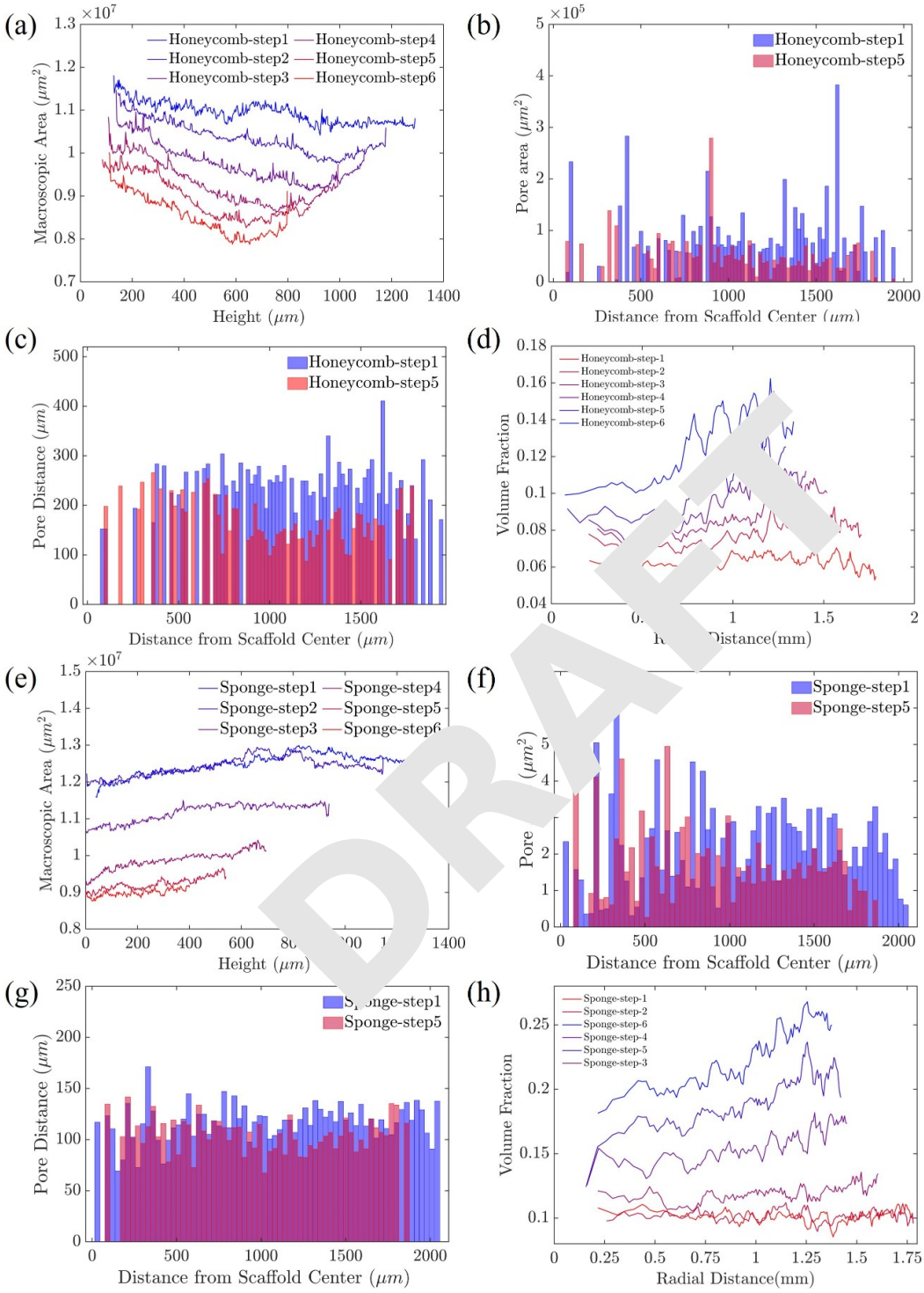

Fig. 4. Evolution of microstructural features of a honeycomb construct with increasing deformation. (a) Macroscopic area as a function of specimen height. (b) Pore area distribution as a function of radial distance in the undeformed ($\lambda = 0$) and deformed ($\lambda = 30.5\%$) configurations. (c) Neighbor distance as a function of radial coordinate in the undeformed ($\lambda = 0$) and deformed ($\lambda = 30.5\%$) configurations. (d) Spatial distribution of volume fraction in different strain levels. Evolution of microstructural features of a sponge construct with increasing deformation. (e) Macroscopic area as a function of specimen height. (f) Pore area distribution as a function of radial distance in the undeformed ($\lambda = 60\%$) and deformed ($\lambda = 0$) configurations. (g) Neighbor distance as a function of radial coordinate in the undeformed ($\lambda = 0$) and deformed ($\lambda = 60\%$) configurations. (h) Spatial distribution of volume fraction in different strain levels.

difference between a typical soft material and these collagen constructs we include in Figure 5(a) the corresponding area evolution of a Neo-Hookean material under compression. The associated deformations for a 40% nominal strain are shown in Figure 5(b). Even though many cellular materials, including elastomeric foams (18) and 3D-printed porous media (19), show negligible expansion in the transverse direction when compressed, the strong area reduction that the collagen scaffolds display, corresponding to a negative tangent Poisson's ratio, is a characteristic seen in a certain class of mechanical metamaterials (20–22) and is associated with improved energy absorption characteristics.

Discussion

In summary, here we present a complete 3D microstructural analysis of soft collagen scaffolds with honeycomb and sponge microstructures under compressive loads. We find that the resulting deformation is highly heterogeneous across the specimen area with the emergence of regions with increased pore compaction driven by elastic instabilities. This compaction is attributed to the microstructural design of collagen scaffolds and the vertically oriented pores with a length scale of ~100µm. While native cartilage shares a similar vertical alignment, the associated length scales are much smaller, with collagen fiber sizes of ~10µm. A feature that could alter the resulting mechanical behavior. Typically, in low-density lattices and porous materials under compression, localization leads to bands of collapsed pores forming at certain slope with respect to the loading surface (18). On contrary, in this work the collapsing pores form peripherally and divide the scaffold in highly deformed pore clusters near the free boundary, and much less distorted regions in the interior of the specimen. This behavior is reminiscent of the presence of floppy modes on the free boundaries of lattice structures (23). The increased compaction of the collapsed pores near the specimen lateral boundary, and the associated contact between neighboring walls could be responsible for obstructing the propagation of buckling towards the interior of the scaffold. More importantly, the cross-sectional area of the collagen scaffolds decreases gradually as compression increases and the collapse of pores progresses. This area reduction is attributed to the inward buckling and folding of the pore walls. At large deformations, corresponding to effective macroscopic strains of 40%, scaffolds' area at their mid-section is reduced by 5-25%. This auxetic behavior, i.e. the displayed contraction/elongation of the material in the transverse direction when compressed/stretched in the longitudinal one, has been reported extensively in cellular solids and in particular those with re-entrant members (24) or chiral mesostructures (25). Since in these materials the resulting negative Poisson's ratio is driven by geometry, there have been efforts (26–28) to exploit these microstructural features in additively manufactured scaffolds for tissue engineering. In contrast to these material systems, the auxetic behavior in the collagen scaffolds examined here is deformation dependent and generated by the elastic instabilities that govern the associated large deformations. Even though these instabilities can potentially lead to beneficial properties (20–22), in the case of collagen scaffolds in cartilage constructs the auxetic behavior may well impede implant integration. To date, the lateral integration of engineered cartilage constructs with host tissue has proven to be a consistent challenge (29). Surprisingly, past in vivo studies have demonstrated that the lateral integration of tissue-engineered cartilage constructs using porous collagen scaffolds is not significantly superior to that achieved through microfracture surgeries (30–32). In microfracture surgeries, insufficient lateral integration often results from the disparity in cartilage types between the newly formed fibrocartilage and the native hyaline cartilage, or incomplete defect fill (33–37). Conversely, tissue-engineered cartilage constructs created from porous scaffolds do not encounter these issues as they are composed of hyaline cartilage and fully occupy the defect. Therefore, the fundamental reason for the persistent challenge in lateral integration of implanted tissue-engineered cartilage constructs remains poorly understood. The lateral contraction of the collagen scaffolds reported here due to auxetic behavior, could result in the formation of a physical gap between the engineered cartilage constructs and the native host tissue. In addition, the increased compaction near the boundary pores can induce cell death (10), resulting in significantly lower cell viability at the vicinity of the free boundary compared to the interior of the engineered construct. Previous studies have indicated that low cell viability at the interface between the graft and the host tissue can hinder the integration process (29, 38, 39). Overall, the auxetic behavior observed in collagen scaffolds provides valuable insights into the underlying reasons for the persistent challenge of lateral integration in tissue-engineered cartilage constructs. It is important to note that the experiments reported here do not aim to replicate the behavior of the complete cartilage constructs in vivo. Doing so would require a different testing setup as well as filling partially the pores of the scaffolds with chondrocytes and matrix, which are left for future studies. Nonetheless, understanding the effect of microstructure on the resulting elastic instability cascade and evolution of collapse in an uncoupled manner from the complex micromechanical environment during implantation is deemed imperative. Furthermore, high-fidelity numerical models that are able to reproduce experimental data and facilitate the exploration of the vast parameter space are also essential for designing novel microstructures. Towards this goal, advances in 3D bio-printing are expected to provide increased control over the structure of synthesized scaffolds, potentially enable the tailoring of morphological features that yield predetermined target deformation modes at the post-buckling regime.

Materials and Methods

Collagen scaffold preparation. Honeycomb (Histogenics Corp., Waltham, MA) and sponge (Koken CO., LTD, Tokyo, Japan) collagen scaffolds were obtained. Both honeycomb and sponge scaffolds were made from type I bovine dermis collagen and had pore sizes ranging from 100 - 200µm in

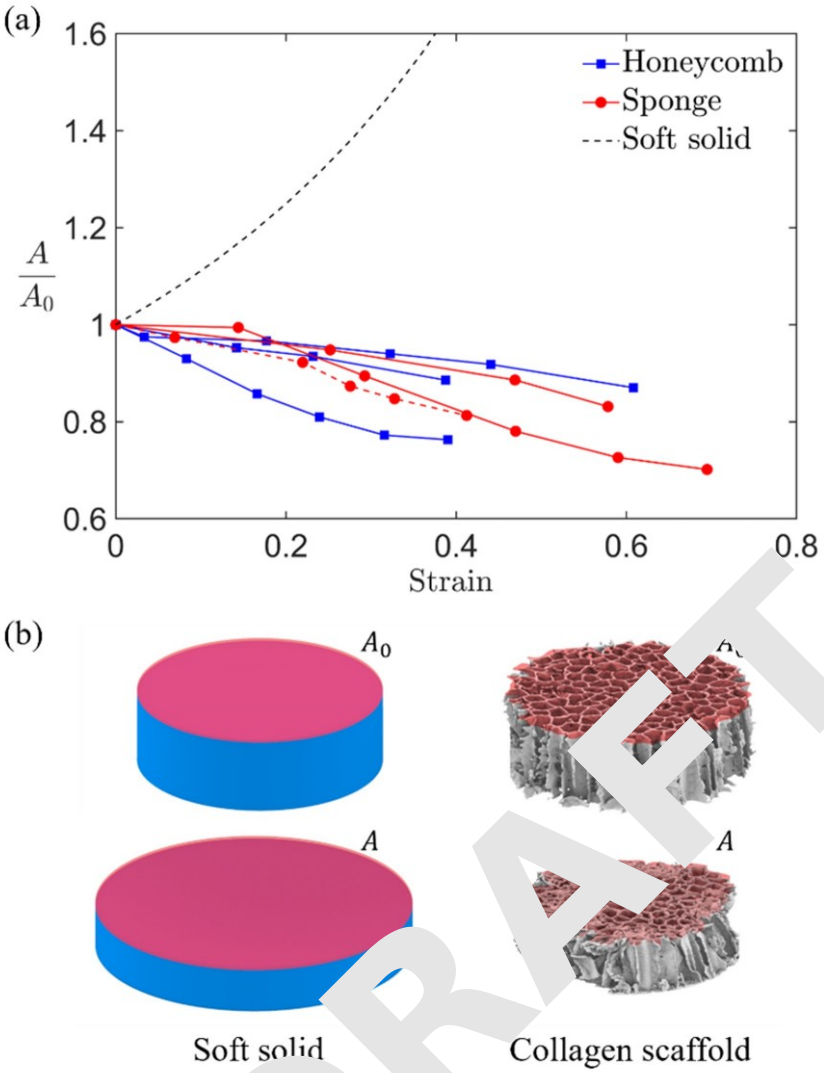

Fig. 5. (a) Evolution of normalized macroscopic area with increasing macroscopic strain for collagen scaffolds with honeycomb and sponge microstructures. For compa the corresponding area evolution of a monolithic soft solid is included. (b) The gradual reduction in the cross-sectional area shows the strong auxetic metamaterial behavior of collagen constructs i.e., the presence of lateral contraction when vertically compressed, instead of the expansion observed in typical soft solids.

diameter and 1.5mm in height, according to manufacturing specifications. A total of 6 samples (3 honeycomb scaffolds and 3 sponge scaffolds) were cut using 4mm and 6mm biopsy punches (Integra York PA, Inc., York, PA) with pores aligned in the axial direction.

Micro-computed tomography. The cellular microstructure of collagen constructs is characterized through µCT using a Skyscan 1172 system (by Bruker). The scanning and imaging settings adopted, based on maximizing accuracy and performance, include 67kV and 174µA power for the X-ray source, projection images over a 180° rotation without any filtering, 2.3µm image pixel size. The projection images underwent flat-field and dark-field corrections for better contrast. After scanning, projection images are reconstructed by the NReconn software with default post-alignment, smoothing, and ring artifact correction settings.

Image analysis and extraction of microstructural characteristics. 2D slices obtained from the reconstructed images are imported into MATLAB for further imaging analysis and extraction of key morphological characteristics. We employ the hysteresis thresholding method to differentiate between collagen and void regions. Following this approach, pixels with intensity values above a user-set upper threshold are classified as solid, while pixels with intensity values below a corresponding low threshold are classified as voids. All pixels with intermediate intensity values are then evaluated based on their connectivity to the pixels corresponding to the solid phase. Here, a pixel connectivity parameter equal to four is chosen. We extract next the distributions of four microstructural characteristics, namely the wall thickness, pore area, compactness, and pore neighbor distance along the height of the scaffold, at four equidistant increments. The wall thickness t around each pore is determined by the bwdist function in MATLAB. The size and shape of each pore are characterized by calculating the corresponding area A and

compactness. The latter is estimated using a ratio of the pore area A and the pore perimeter P i.e., "compactness" = $\frac{4\pi \times A}{P^2}$. The pore "density" is evaluated through the neighbor distance metric i.e., the length between the centroids of two adjacent pores. All of the above calculations require distinct boundaries for all pores, that we achieve here by skeletonizing the binary 2D images using the bwboundaries function in MATLAB. For the 3D visualization and image analysis, the binary image stack is exported to ImageJ where, using the 3D viewer function with a resampling factor of two, a surface mesh is generated. The mesh is then exported as an STL file into Rhino3D for visualization.

In-situ testing. We conduct a series of in-situ compression experiments under displacement control using an MTS loading stage with a 44N load cell. In each test, the specimen is placed in the center of the stage and subsequently an upward displacement with a rate (~0.5mm/min) is prescribed on the bottom platen to ensure quasi-static compaction. Once the specimen comes to full initial contact with the platen, the scaffold is scanned and its undeformed microstructure is extracted. Subsequently each specimen is compressed in increments of average macroscopic strain of 7.5%. At the end of each loading increment, testing is paused, and the specimen is scanned, keeping the image acquisition settings consistent. These steps are iterated until each specimen reaches an average macroscopic compaction of 40%. We note here a set of three samples for each cellular microstructure i.e., for the honeycomb and sponge constructs.

Deformation-dependent morphological features. Through the in-situ testing of the collagen scaffolds, we further calculate the evolution of morphological characteristics as a function of the applied loading and resulting deformation. In addition to the aforementioned pore-related features, here we also measure how increased compression affects two additional microstructure properties: (a) the sectional area of each specimen across their height and (b) the volume fraction as a function of radial distance from the specimen center. Regarding the former, we first calculate the sectional area centroid of the scaffold by averaging the binary image with its position, and then create 100 circumferential curves from the center to the image boundary. Subsequently, we calculate the outer intersection point between each curve and the scaffold. We connect all these intersection points in a right-handed order to form a closed domain and measure the corresponding area. For the latter part, the spatial distribution of the volume fraction was quantitatively assessed using a sliding box approach on binary image stacks of the scaffold from the scanning. A three-dimensional box of a predefined x-y size (460µm) was systematically slid across this binary domain in the x-y plane with a specific stride (230µm), spanning the entire depth of the stack in the z-dimension to ensure comprehensive assessment across the scaffold's height. For each box, the volume fraction was determined as the ratio of voxels of the scaffold to the total number of voxels in the box. Simultaneously, the Euclidean distance between the center of each box and the scaffold's central point was calculated. This approach enabled a quantitative analysis of the heterogeneous compaction of the scaffold during the compression.

ACKNOWLEDGEMENTS

The authors would like to thank Robert C. Spiro (Aesculap Biologics, LLC) for helpful discussions.

Funding: This work was supported by National Science Foundation Award #2129825 (EC, SG) National Science Foundation Award #2129776 (BK, NB, LJB).

Author contributions: Conceptualization: NB, LJB, SG Investigation: EC, BK Supervision: NB, LJB, SG Funding acquisition: NB, LJB, SG Writing—original draft: EC, BK Writing—review & editing: EC, BK, NB, LJB, SG

Competing interests: The authors declare no conflict of interest.

Data and materials availability: All data needed to evaluate the conclusions in the paper are present in the paper and/or the Supplementary Materials.

Bibliography

1. Hee Kwon, William E Brown, Carrie A Lee, Doris Wang, Nicholas Paschos, Jerry C Hu, and Kyriacos A Athanasiou. Surgical and tissue engineering strategies for articular cartilage and meniscus repair. Nature Reviews Rheumatology, 15(9):550–570, 2019.
2. Alan Nixon, Eric Rickey, Timothy Butler, Melissa Scimeca, Nicholas Moran, and Gina Pennella. A chondrocyte infiltrated collagen type i/iii membrane (maci® implant) improves cartilage healing in the equine patellofemoral model. Osteoarthritis and Cartilage, 23 (4):648–660, 2015.
3. Lukas Zinner, Christina Albrecht, Brigitte Wondrasch, Heinz Widhalm, Georg Vekszler, Siegfried Trattnig, Stephan Marlovits, and Stefan Aldrian. Results 2 years after matrix-associated autologous chondrocyte transplantation using the novocart 3d scaffold: an analysis of clinical and radiological data. The American Journal of Sports Medicine, 42(7): 1618–1627, 2014.
4. Michael S Kane, Russell J Williams III, Thomas M DeBerardino, Douglas Taylor, Calvin B Chapman, Eric E Anderson, and David C Crawford. Review of an exploratory phase 1 da regulated clinical trial of a novel surgical innovation: completion of a prospective, randomized, controlled trial to compare neocart with the standard-of-care, microfracture, for articular cartilage lesions. Annals of Joint, 3, 2018.
5. Allison M Bailey, Michael Mendicino, and Peggy Au. An fda perspective on preclinical development of cell-based regenerative medicine products. Nature Biotechnology, 32(8):721–723, 2014.
6. Jaimin M Patel, Brian C Wise, Elizabeth D Bonnevie, and Robert L Mauck. A systematic review and guide to mechanical testing for articular cartilage tissue engineering. Tissue Engineering Part C: Methods, 25(10):593–608, 2019.
7. Jennifer M Middendorf, Sonya Shortkroff, Charles Dugopolski, Sean Kennedy, John Siemiatkoski, Lawrence R Bartell, Itai Cohen, and Lawrence J Bonassar. In vitro culture increases mechanical stability of human tissue engineered cartilage constructs by prevention of microscale scaffold buckling. Journal of Biomechanics, 64:77–84, 2017.
8. Byumsu Kim, Tanya-Anne N Kelly, Hyung-Jin Jung, Olivia S Beane, Sarindr Bhumiratana, Nikolaos Bouklas, Itai Cohen, and Lawrence J Bonassar. Microscale strain concentrations in tissue-engineered osteochondral implants are dictated by local compositional thresholds and architecture. Journal of Biomechanics, 162:111882, 2024.
9. Lawrence R Bartell, Lisa A Fortier, Lawrence J Bonassar, and Itai Cohen. Measuring microscale strain fields in articular cartilage during rapid impact reveals thresholds for chondrocyte death and a protective role for the superficial layer. Journal of Biomechanics, 48 (8):1440–1446, 2015.
10. Byumsu Kim, Nikolaos Bouklas, Itai Cohen, and Lawrence J Bonassar. Instabilities induced by mechanical loading determine the viability of chondrocytes grown on porous scaffolds. Journal of Biomechanics, 152:111591, 2023.
11. Katia Genovese, Sjoerd Leeflang, and Amir A Zadpoor. Microscopic full-field three-dimensional strain measurement during the mechanical testing of additively manufactured porous biomaterials. Journal of the Mechanical Behavior of Biomedical Materials, 69:327–341, 2017.
12. Bo Wang, Lu Sun, and Bing Pan. Mapping internal deformation fields in 3d printed porous structures with digital volume correlation. Polymer Testing, 78:105945, 2019.
13. Hiroshi Itoh, Yoshio Aso, Michiko Furuse, Yoshihiko Noishiki, and Tatsuo Miyata. Honeycomb collagen carrier for cell culture as a tissue engineering scaffold. Artificial Organs, 25 (6):511–517, 2001.
14. Sonya Shortkroff, Laurence JB Tarrant, Eric J Roos, Robert Lane Smith, and Hans PI Claesson. Method for use of a double-structured tissue implant for treatment of tissue defects, 2013. US Patent 8,371,399.
15. Reza Bostanabad, Yi Zhang, Xingjie Li, Thomas Kearney, L. Catherine Brinson, Daniel W Apley, Wing Kam Liu, and Wei Chen. Computational microstructure characterization and reconstruction: Review of the state-of-the-art techniques. Progress in Materials Science, 95:1–41, 2018.
16. Haifeng Xu, Ren Liu, Alok Choudhary, and Wei Chen. A machine learning-based design representation method for designing heterogeneous microstructures. Journal of Mechanical Design, 137(5):051403, 2015.
17. Guillermo Requena, Georg Fiedler, Bernhard Seiser, Hans Peter Degischer, Marco Di Michiel, and Thierry Buslaps. 3d-quantification of the distribution of continuous fibres in unidirectionally reinforced composites. Composites Part A: Applied Science and Manufacturing, 40(2):152–163, 2009.
18. Chi Luan, Andrew M Kraynik, and Stavros Gaitanaros. Microscopic and macroscopic instabilities in elastomeric foams. Mechanics of Materials, 164:104124, 2022.
19. Katia Bertoldi, Mary C Boyce, Sebastien Deschanel, Stefanie M Prange, and Tom Mullin. Mechanics of deformation-triggered pattern transformations and superelastic behavior in

periodic elastomeric structures. Journal of the Mechanics and Physics of Solids, 56(8): 2642–2668, 2008.
20. Arnaud Lazarus and Pedro M Reis. Soft actuation of structured cylinders through auxetic behavior. Advanced Engineering Materials, 17(6):815–820, 2015.
21. Jee Shim, Shian Shan, Andrej Košmrlj, Sung H Kang, E Rain Chen, James C Weaver, and Katia Bertoldi. Harnessing instabilities for design of soft reconfigurable auxetic/chiral materials. Soft Matter, 9(34):8198–8202, 2013.
22. Shapour Babaee, Jee Shim, James C Weaver, E Rain Chen, Neil Patel, and Katia Bertoldi. 3d soft metamaterials with negative poisson's ratio. Advanced Materials, 25(36):5044–5049, 2013.
23. Charles L Kane and T C Lubensky. Topological boundary modes in isostatic lattices. Nature Physics, 10(1):39–45, 2014.
24. Roderic Lakes. Foam structures with a negative poisson's ratio. Science, 235(4792):1038–1040, 1987.
25. Dennis Prall and Roderic S Lakes. Properties of a chiral honeycomb with a poisson's ratio of -1. International Journal of Mechanical Sciences, 39(3):305–314, 1997.
26. Joshua J Warner, Adam R Gillies, Han H Hwang, Hong Zhang, Richard L Lieber, and Shaochen Chen. 3d-printed biomaterials with regional auxetic properties. Journal of the Mechanical Behavior of Biomedical Materials, 76:145–152, 2017.
27. Prabhas Soman, Jin Woo Lee, Ameya Phadke, Shyni Varghese, and Shaochen Chen. Spatial tuning of negative and positive poisson's ratio in a multi-layer scaffold. Acta Biomaterialia, 8(7):2587–2594, 2012.
28. Marija Kapnisi, Claire Mansfield, Camille Marijon, Arnaud G Guex, Francesca Perbellini, Ilaria Bardi, Elizabeth J Humphrey, Jennifer L Puetzer, Damia Mawad, Demetrius C Koutsogeorgis, et al. Auxetic cardiac patches with tunable mechanical and conductive properties toward treating myocardial infarction. Advanced Functional Materials, 28(21):1800618, 2018.
29. Imran Khan, Samantha Gilbert, Sim K Singhrao, Victor Duance, and Charles W Archer. Evaluation of the reasons for failure of integration during cartilage repair. a review. eCM, 16: 26–39, 2008.
30. Gunnar Knutsen, Jon O Drogset, Lars Engebretsen, Thor Grontvedt, Vidar Isaksen, Tor C Ludvigsen, Steven Roberts, Eirik Solheim, Tore Strand, and Oyvind Johansen. A randomized trial comparing autologous chondrocyte implantation with microfracture: findings at five years. JBJS, 89(10):2105, 2007.
31. Guang-Hui Gou, Fu-Jen Tseng, Shang-Hsiu Wang, Po-Jen Chen, Jen-Fu Shyu, Chia-Feng Weng, and Rong-Yuan Pan. Autologous chondrocyte implantation versus microfracture in the knee: a meta-analysis and systematic review. Arthroscopy: The Journal of Arthroscopic & Related Surgery, 36(1):289–303, 2020.
32. Dieter Van Assche, Filip Staes, Dirk Van Caspel, Johan Vanlauwe, Johan Bellemans, Daniel B Saris, and Frank P Luyten. Autologous chondrocyte implantation versus microfracture for knee cartilage injury: a prospective randomized trial, with 2-year follow-up. Knee Surgery, Sports Traumatology, Arthroscopy, 18(4):486–495, 2010.
33. David D Frisbie, Gary W Trotter, Barbara E Powers, William G Rodkey, J Richard Steadman, Robert D Howard, Ronald D Park, and Charles W McIlwraith. Arthroscopic subchondral bone plate microfracture technique augments healing of large chondral defects in the radial carpal bone and medial femoral condyle of horses. Veterinary Surgery, 28(4):242–255, 1999.
34. Kai Mithoefer, Travis McAdams, Russell J Williams, Peter C Kreuz, and Bert R Mandelbaum. Clinical efficacy of the microfracture technique for articular cartilage repair in the knee: an evidence-based systematic analysis. The American Journal of Sports Medicine, 37(10): 2053–2063, 2009.
35. Michael Endres, Karsten Neumann, Thomas Häupl, Christoph Erggelet, Jochen Ringe, Michael Sittinger, and Christian Kaps. Synovial fluid recruits human mesenchymal progenitors from subchondral spongious bone marrow. Journal of Orthopaedic Research, 25 (10):1299–1307, 2007.
36. Rimtautas Gudas, Rimas J Kalesinskas, Vytautas Kimtys, Edmundas Stankus, Vytautas Toliusis, Giedrius Bernotavičius, and Arūnas Smailys. A prospective randomized clinical study of mosaic osteochondral autologous transplantation versus microfracture for the treatment of osteochondral defects in the knee joint in young athletes. Arthroscopy: The Journal of Arthroscopic & Related Surgery, 21(9):1066–1075, 2005.
37. Peter Christian Kreuz, Christoph Erggelet, Matthias R Steinwachs, Sandra Jeannette Krause, Andreas Lahm, Philipp Niemeyer, Mohamed Ghanem, Martin Uhl, and Norbert Südkamp. Is microfracture of chondral defects in the knee associated with different results in patients aged 40 years or younger? Arthroscopy: The Journal of Arthroscopic & Related Surgery, 22(11):1180–1186, 2006.
38. Andrew Trengove, Cosimo DiBella, and Anthony J O'Connor. The challenge of cartilage integration: Understanding a major barrier to chondral repair. Tissue Engineering Part B: Reviews, 28(2):114–128, 2022.
39. Charles W Archer, Samuel Redman, Imran Khan, James Bishop, and Karen Richardson. Enhancing tissue integration in cartilage repair procedures. Journal of Anatomy, 209(4): 481–493, 2006.